Size Effect on FRP External Reinforcement and Retrofit of Concrete Structures

Abdullah Dönmez, Ph.D.[1]; Mohammad Rasoolinejad, Ph.D.[2]; and Zdeněk P. Bažant, Ph.D., S.E., Hon.M.ASCE[3]

Abstract: The size effect on the strength of reinforced concrete (RC) beams flexurally strengthened by surface bonded sheets of fiber-reinforced polymer (FRP) is studied. As the failure is neither ductile nor brittle, but quasibrittle, occurring after stable growth of large cracks with large damage zones, the transitional size effect governed by the energetic size effect law (SEL) must be expected, which the present analysis confirms. Owing to scarcity of size effect experimental data, finite element (FE) analysis is used. A powerful microplane damage constitutive model M7 for concrete, coupled with the crack band model to suppress spurious mesh sensitivity, is calibrated by fitting the existing test data to FRP-strengthened RC specimens of diverse types, and consequently is trusted to simulate the size effect. The analysis captures the debonding near the concrete–FRP interface starting at midspan or at the end of the FRP sheet. It also captures the debonding between adjacent concrete shear cracks, and the delamination of concrete cover. The causes of these different delamination modes are explained. Simple beam-type formulas, in which the size characteristic is not the beam depth but the length of the shear span, are proposed and validated by FE results. The use of single-lap shear tests to determine the bond strength is critically discussed. Finally, a good fit of a few existing limited test data on the size effect of FRP-strengthened specimens is demonstrated. **DOI: 10.1061/(ASCE)CC.1943-5614.0001070**.

Introduction

Fiber-reinforced polymer (FRP) sheets, serving as external (skin) strengthening of concrete structures and as retrofit of structures damaged, e.g., by earthquake, have been investigated for several decades (Saadatmanesh and Ehsani 1991; Arduini and Nanni 1997). Increasing the flexural capacity of reinforced concrete (RC) beams or structural members with the FRP sheets is a common practice. However, the strength prediction of this type of composite system is not as easy as thought in engineering practice.

The performance of external reinforcement depends on many factors, such as the strength and stiffness of the concrete and FRP, interface strength, geometrical characteristics, and the design details (ACI 440.2R-17; ACI 2017). The variation of the parameters affects the governing failure modes of FRP-strengthened RC members. The main failure modes of these structures are FRP debonding, FRP rupture, concrete crushing at the compression face, and yielding of flexural reinforcement. Several failure modes may proceed simultaneously. Although, based on simulations, only one mechanism dominates the deformation growth at the peak load, the load-bearing capacity of the structures depends on all the failure mechanisms.

The breakage of the FRP–concrete bond, called debonding, is the failure mode considered here to control the peak load (P_{max}). There are several types of debonding failures, as elucidated by Maalej and Bian (2001), Brena et al. (2003), Chiew et al. (2007), and Attari et al. (2012). The failure definitions vary. Here the term "debonding" refers to all the different delamination types, shown in Fig. 1. They are the midspan debonding, intermediate-crack (IC) debonding, end-crack (EC) debonding, cover delamination, and cover tooth delamination (Fig. 1). These debonding types differ in the initiation point of failure, the triggering effects, the amount of debris on the FRP surface after delamination, and the fracture growth mechanism. As the bond at the FRP–concrete interface is generally strong enough, the debonding crack occurs not at the FRP surface but inside the concrete just next to that surface (unless the FRP was installed improperly). Therefore, the strength of concrete substrate is important for the load capacity.

If the failure mechanisms were ductile and the failure obeyed plastic limit analysis, the nominal strength σ_N of geometrically similar structures, defined as the maximum load divided by any chosen homologous cross-sectional area, would be independent of the structures size, D, which is called the case of no size effect. If the failure occurred by brittle propagation of a sharp (point-wise) crack tip, then the size effect of linear elastic fracture mechanics (LEFMs), i.e., $\sigma_N \propto D^{-1/2}$, would apply. However, because the failure mechanisms are between ductile and brittle, i.e., quasibrittle, consisting of the growth of large damage zones, the size effect on σ_N is a transition between the two special cases (Bažant 1984; Bažant and Planas 1998; Bažant 2002; Dönmez and Bažant 2017). Therefore, the failure of the FRP–concrete interface should be calculated via quasibrittle fracture mechanics, and the size effect needs to be considered in design.

Beam-Type Formulation and Assumptions

Normally, RC beams should designed so that the load that causes ductile failure by yielding of flexural reinforcing bars would be smaller than the load that causes brittle failure of concrete. In that

[1]Postdoctoral Research Fellow, Dept. of Civil and Environmental Engineering, Northwestern Univ., Evanston, IL 60208; Dept. of Civil Engineering, İstanbul Teknik Univ., Istanbul, 34469, Turkey. Email: donmezab@itu.edu.tr

[2]Postdoctoral Research Fellow, Northwestern Institute on Complex Systems, Northwestern Univ., Evanston, IL 60208. ORCID: https://orcid.org/0000-0003-3387-3580. Email: rasoolinejad@u.northwestern.edu

[3]McCormick Institute Professor and W.P. Murphy Professor of Civil and Mechanical Engineering and Materials Science, Northwestern Univ., Evanston, IL 60208 (corresponding author). Email: z-bazant@northwestern.edu

Note. This manuscript was submitted on January 28, 2020; approved on June 2, 2020; published online on August 6, 2020. Discussion period open until January 6, 2021; separate discussions must be submitted for individual papers. This paper is part of the ***Journal of Composites for Construction***, © ASCE, ISSN 1090-0268.

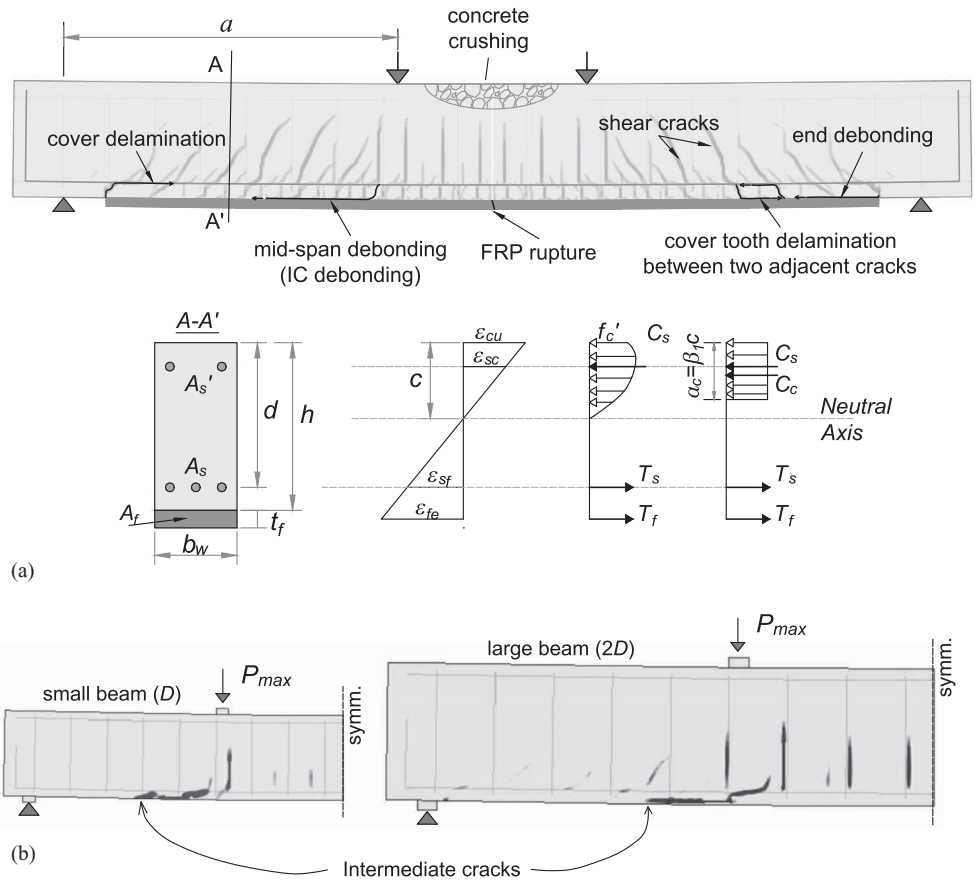

Fig. 1. Description of the FRP reinforcement and failure modes.

case, the size effect is avoided. However, it cannot be avoided when the beam is externally strengthened by bonded FRP plates.

In the design guidelines, such as the ACI 440.2R-17 report (ACI 2017), the ultimate load capacity of an FRP-strengthened RC beam under flexure is calculated based on the assumption of rectangular stress distribution with resulting compression C_c as shown in Fig. 1, subject to various restrictions. Compressive force C_s due to compression reinforcement, if any, must be included. Crushing of concrete is assumed to occur when the concrete reaches a limit strain, approximated as $\varepsilon_{cu} = 0.003$. In general, concrete is assumed to have negligible tensile resistance, and so only the tensile forces due to flexural steel, T_s, and the bonded FRP layer, T_f, are considered. The flexure produces tension in the bonded FRP sheet. The ultimate bending moment is

$$M_d = M_s + M_f \tag{1}$$

where M_s, M_f are the moment contributions from flexural steel reinforcement and the FRP. According to the ACI 440.2R-17 report, the additional flexural strength, M_f, due to the FRP reinforcing layer is calculated from the effective stress, f_{fe}, in the FRP (ACI 2017):

$$M_f = \psi_f A_f f_{fe}\left(h - \frac{1}{2}\beta_1 c\right) \tag{2}$$

where ψ_f, β_1 are empirical factors, and both equal to 0.85.

The effective stress, f_{fe}, is the maximum stress that FRP can resist, and is calculated as

$$f_{fe} = E_f \varepsilon_{fe}; \quad \varepsilon_{fe} = \varepsilon_{cu}(h - c)/c - \varepsilon_i \le \varepsilon_{fd} \tag{3}$$

Here E_f is the Young's modulus of FRP, c is the depth from top face to the concrete compression resultant, and ε_i is the initial strain of concrete at the moment of FRP installation. The effective FRP design stress f_{fd} is limited by the design strain, ε_{fd}, which is specified as

$$f_{fd} = E_f \varepsilon_{fd}; \quad \varepsilon_{fd} = \alpha\sqrt{f_c'/nE_f t_f} \le 0.9\varepsilon_{fu} \tag{4}$$

Here α is an empirical factor equal to 0.41 (0.083 in the United States customary system or USCS), n is the layer number (ply number), and t_f is the FRP sheet thickness. The design strength, f_{fd}, is lower than the tensile strength of FRP, f_{fu}. Aside from the safety factors, the type of surface treatment, the shear strains in the bonding (adhesive) layer, the relative slips between the concrete and FRP sheets, and the imperfections on the bonding surface are neglected in design. The main reason for the limitation of the effective stress (or strain) is the strength of the concrete substrate.

Eq. (4) is a modified version of the Teng et al.'s (2003) model, which is based on the effective bond length concept deduced from single-lap shear tests (SSTs). According to this concept, there exists an effective bond length beyond which a further increase of the bonding length will have no effect on beam strength.

Generalization of Simplified Beam-Type Analysis for Fracture Size Effect

To take into account the fracture size effect, a different approach to the strength of RC members reinforced by FRP sheets is proposed here. Because the fracture process zones (FPZs) are large (approximately 0.5 m for concrete, but only about a few micrometers for metals), i.e., nonnegligible compared with the cross-sectional dimensions of the structure, the size effect on the mean nominal structure strength, σ_N, must be expected to be of the energetic (rather than

statistical) type, and because large cracks develop before the maximum load, the size effect must be of type 2, which is most easily demonstrated by the dimensional analysis of energy balance (see A3 in Dönmez and Bažant 2019). This means that, to obtain the nominal strength σ_N for any structure size D, the nominal strength, σ_{N0}, due to concrete and FRP calculated by the traditional strength theory (or limit analysis) should be multiplied by the size effect factor λ_s, i.e.,

$$\sigma_N = \sigma_{N0}\lambda_s, \quad \lambda_s = (1 + a/D_0)^{-1/2} \tag{5}$$

Here D_0 = constant = transitional structure size, and a = shear span (factor λ_s has been introduced in 2019 into the provisions for beam shear, punching, and strut-and-tie model of ACI design code ACI-318-2019). For FRP reinforcement, σ_N needs to be based on the shear span and on web width b_w, and σ_{N0} is defined empirically as in classical analysis:

$$\sigma_N = P_{\max}/ab_w, \quad \sigma_{N0} = \beta\gamma\sqrt{f_c'} \tag{6}$$

$$\text{where } \beta = 1 + \alpha_1\xi^{n_1} - \alpha_2\xi^{n_2} \geq 1.1, \quad \xi = \frac{E_f I_f}{E_s I_s} \tag{7}$$

Here E_c, E_s = Young's moduli of concrete and steel; γ = empirical correction factor; I_f, I_s = moments of inertia about the neutral axis of the transformed cross sections of FRP and steel reinforcements, respectively; $\alpha_1 = 1.1$, $\alpha_2 = 2.5$, $n_1 = 0.5$, and $n_2 = 2$. The empirical parameters in Eqs. (5)–(7) need to be calibrated by fitting the database.

Validation and Calibration of Microplane Finite Element Model by Test Data

There are no experimental data available to validate and calibrate the described model. Therefore, similar to other recent successful studies, a realistic constitutive and fracture model is validated and calibrated by experimental data that exist. The model is then used to predict the size and shape effects through computer finite element (FE) simulations.

As a realistic damage constitutive model, the microplane model M7 (whose coding can be freely downloaded from the corresponding author's website) is chosen. M7 is the latest in a series of microplane models for concrete developed at Northwestern University (Caner and Bažant 2013a). The material properties are characterized by a relation between the stress and strain components (or forces and displacements) on the microlevel (Bažant and Ožbolt 1990) (or, more precisely, the mesolevel). The stress–strain relations are defined not in terms of the macrolevel continuum tensors, but in terms of the stress and strain vectors on planes of all possible orientations within the material, called the microplanes.

The microplane model, M7, which is designed for an explicit numerical algorithm, has been shown to be capable of realistically predicting the concrete damage behaviors over a broad range of loading scenarios (Caner and Bažant 2013b; Dönmez and Bažant 2017; Rasoolinejad and Bažant 2019). It is always convergent, robust, and has been applied in dynamic problems with more than 3×10^7 unknowns (nodal displacements or degrees of freedom). The present simulations are performed on ABAQUS, where M7 is inserted as a user's material subroutine VUMAT.

To prevent spurious mesh sensitivity, the crack band model is used as the localization limiter (Bažant and Oh 1983). To minimize accuracy loss due to scaling of the postpeak, a constant element size h_c (equal approximately to 1–2 times the maximum aggregate size) is adopted for structures of all sizes. All the computations include eight-node hexahedral elements for concrete and two-node beam elements in 3D space for steel reinforcement. The FRP material is modeled by four-node shell elements. Because the response of FRP material is almost linear until rupture, a linear elastic behavior is adopted in the numerical analyses for the FRP plates. Perfect bonding features between the concrete–FRP sheet and concrete–reinforcing steel bars are assumed and implemented in the numerical analyses. To calibrate the free parameters of M7, FE program with M7 is optimally fitted to all relevant available test data. The adjustable parameters of M7 sufficed to match the main properties, i.e., the post-peak behavior, fracture energy, and strength values. The steel is modeled as a bilinear elasto-plastic or hardening plastic material. The FRP materials, both carbon fiber-reinforced polymer (CFRP) and glass fiber-reinforced polymer (GFRP), are simulated as linear elastic up to rupture.

Single-Lap Shear Test

The bond characteristics of the FRP–concrete interface have generally been assessed by SSTs [Fig. 2(a)]. In SSTs, the tension in the FRP is transferred to the concrete substrate by bond shear stresses of rather nonuniform stress distribution. Most of the FRP–concrete interface does not contribute strongly to resisting the transverse shear force in the beam. Only a certain active zone of effective length L_e within the total bonding length L_b does. Once the shear stress of the concrete substrate reaches the strength value, cracking

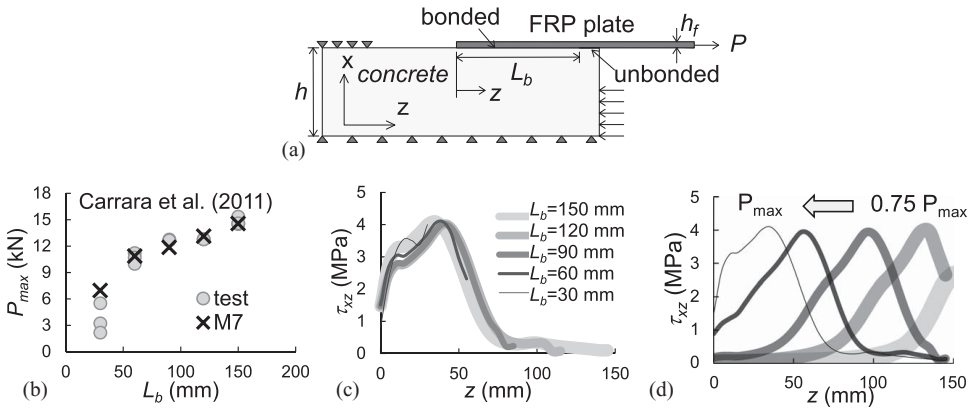

Fig. 2. (a) Schematic description of SSTs; (b) calibration of M7 by using the test data by Carrara et al. (2011); (c) shear stress distribution along the bonding length for various L_b values prior to failure; and (d) the variation of the shear stress pattern with loading for $L_b = 150$ mm.

J. Compos. Constr., 2020, 24(5): 04020056

begins inside this zone. When L_b exceeds L_e, the active stress transfer begins to shift towards the endpoint of L_b. The maximum load P_{max} drops roughly when zone L_e cannot propagate any further.

The FE results illustrate the shear failure mechanism of SST. The calibration of M7 is based on the test data of Carrara et al. (2011), as shown in Fig. 2(b). The simulations of the test data include various bonding lengths of five different SST specimens which are $L_b = 30$, 60, 90, 120, and 150 mm. The dimensions of the concrete prism are $150 \times 90 \times 300$ mm^3. The compressive strength of the concrete is 37.2 MPa and tensile strength 4.8 MPa. The CFRP plate used measures 1.3 mm in thickness and 50 mm in width. Fig. 2(c) shows the shear stress distributions at P_{max} along the CFRP–concrete interface, for five L_b values. As can be seen in Fig. 2(c), the short bonding lengths are not sufficiently long to fully develop L_e. Nonetheless, the distribution of the shear stresses shows very similar patterns along the length from the endpoint of the bond (z). The length of an active bond zone, in which the shear stresses transfer the tension forces on the FRP, does not change with the total bonding length but remains constant for all L_b values, as noted in previous studies (Chen and Teng 2001). The progress of the shear stress distribution for $L_b = 150$ mm until the complete failure is shown in Fig. 2(d). The active shear zone germinates at the nearest point to the applied load. After reaching the strength threshold of the material, the effective interface zone shifts away from the fractured concrete surface. Finally, failure under load control occurs when the end of the FRP sheet begins to restrict the active zone length.

The effective bonding length, L_b, is expected to be a function of the stiffnesses of the bonded materials. The shear strength of SST specimens is a function of L_b and the fracture energy, G_f, of the concrete. However, the application of the SST models to the debonding failures of FRP-reinforced members under flexure is questionable, as we show next by FE analysis.

Flexural Strengthening of RC Beams with FRP

The FE program simulating the FRP-strengthened RC beams under flexure is used to fit the test data sets from different studies. In the tests of Maalej and Bian (2001), four layers (or sheets) of different thicknesses are used to strengthen the RC beams. One layer of a CFRP sheet has a thickness of 0.111 mm. The RC beams contain both flexural and shear steel-reinforcement and have a cross-sectional dimensions of 150×115 mm^2. The concrete cover is 31 mm thick and the FE size is 20 mm. The control beam specimen with no FRP reinforcement fails by steel bar yielding, followed by concrete crushing. The specimen with 1 FRP layer (1L) fails by debonding at midspan (IC debonding); for two layers (2L), by end debonding and IC debonding; for three (3L) and four layers (4L) by delamination followed by end debonding. The FE simulations confirm that a slightly different failure load can correspond to very different failure modes. For example, the 1L specimen in Maalej and Bian (2001) failed by FRP rupture, but FE analysis shows that the 1L specimens failing by FRP rupture and by IC debonding have very similar peak loads. Therefore, the elastic behavior of the FRP must be modeled accurately.

The results of M7 calibration by the load-deflection curves are shown in Fig. 3(a). The solid curves show the FE results, and the circle points the test results. Based on this calibration, the responses of RC beams with more FRP layers are computed. Fig. 3(b) shows the experimental and computed normalized strength values as a function of the number of layers (i.e., of CFRP thickness). The normalization is defined according to the unstrengthened case. Thus, σ_0 refers to the strength of the control specimen computed according to Eq. (6). Fig. 3(b) shows that, initially, the strength of FRP-reinforced RC beams increases with the number of layers. However, increasing the FRP thickness changes the stiffness difference between the FRP-strengthened and unstrengthened RC beams. Therefore, the FRP-cutoff point (plate curtailment) causes a change of the failure mode for higher thicknesses of FRP sheets. In general, thin FRP layers fail by IC debonding, and thick layers fail by end debonding or cover delamination.

An additional increase of the FRP layer produces a high tensile stress concentration at the FRP end (the cutoff point). The tensile stress distribution determines the failure mode change from debonding to cover delamination. An increase of the stiffness ratio for these two modes leads causes the concrete cover to be ripped off due to high tensile stresses at the sheet cutoff zone. This is why, after a certain specific stiffness, additional FRP reinforcement does not strengthen the beam, as seen in Fig. 3(b). The stiffness

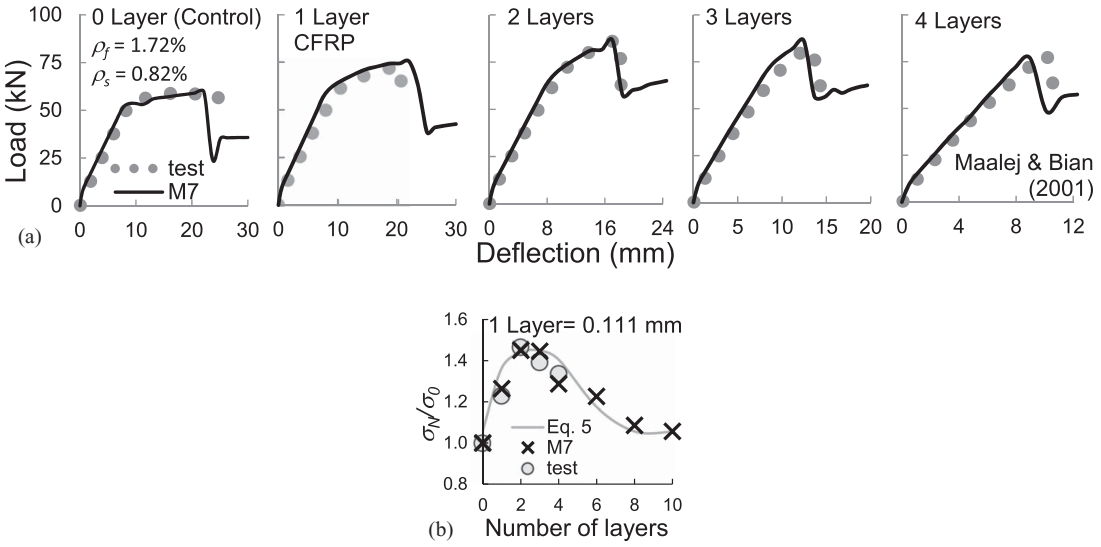

Fig. 3. FRP-reinforced RC beams: (a) test data and calibration of M7 using the first data set (Maalej and Bian 2001); and (b) prediction for higher thicknesses of CFRP ($\sigma_0 = 0.52$ MPa).

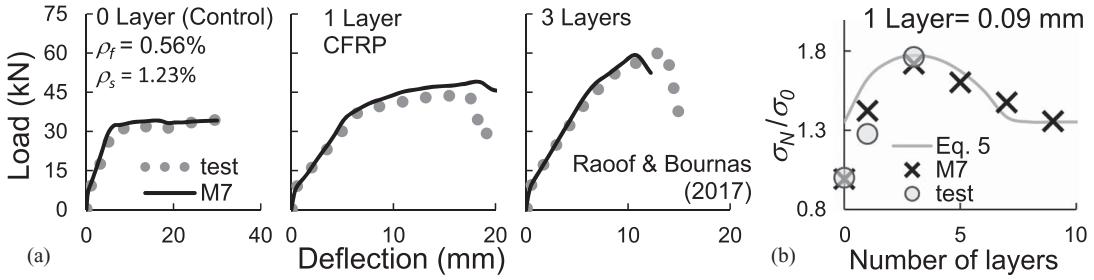

Fig. 4. (a) Calibration of M7 by the second data set (Raoof and Bournas 2017); and (b) predictions for higher thicknesses ($\sigma_0 = 0.29$ MPa).

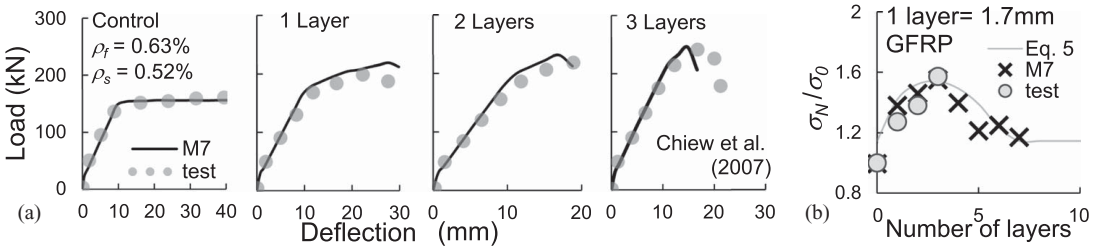

Fig. 5. (a) Calibration of M7 by the third data set (Chiew et al. 2007) with GFRP reinforcement; and (b) prediction for higher thicknesses ($\sigma_0 = 0.49$ MPa).

ratio, ξ, in Eq. (7) can be used to distinguish the various debonding failure modes. The optimal fit of Eq. (5) to the computed data is obtained by substituting 1.1, 3.0, 0.5, and 2 for α_1, α_2, n_1, and n_2, respectively [Fig. 3(b)].

The calibration result based on the second data set is shown in Fig. 4(a) (Raoof and Bournas 2017). Here the RC beam specimens strengthened with one and three layers of CFRP are used in the calibration. The beams have a rectangular cross-section with dimensions of $h \times b_w = 203 \times 102$ mm^2, and the shear span is $a = 580$ mm. The thickness of the concrete cover is 27 mm and the element size $h_c = 20$ mm. The flexural steel reinforcement ratio is $\rho_f = 0.56\%$, and the shear reinforcement (stirrups) ratio $\rho_s = 1.23\%$. The control specimen (with 0 layers) fails by yielding of flexural steel followed by concrete crushing on the compression face. The intermediate (midspan) cracks trigger the delamination failure of the 1L beam. The main failure mode of the 3L beam is a mix of IC debonding and end debonding. Fig. 4(b) also shows the result of extrapolation to higher thicknesses. The nominal strength of the strengthened member decreases when the number of layers is greater than three, which corresponds to the critical value of $\xi = 0.35$. Another data set with M7 calibration is based on the tests of RC beams strengthened with sheets of GFRP (Chiew et al. 2007) [Fig. 5(a)]. The beams are strengthened with one, two, and three layers of GFRP sheets. The cross-sectional dimensions are 350×200 mm^2 ($h \times b_w$) and the span is $a = 800$ mm. The thickness of the concrete cover is 33 mm and the element size $h_c = 25$ mm. The flexural and shear steel reinforcement ratios are $\rho_f = 0.63\%$ and $\rho_s = 0.52\%$, respectively. The control specimen (zero layers) fails by yielding of flexural steel followed by concrete crushing on the compression face. The intermediate (midspan) cracks trigger the delamination failure of the beams with one and two layers of GFRP. The main failure mode of the beam with three layers is a mix of IC debonding and end debonding. Fig. 5(b) shows the extrapolation for higher thicknesses and the variation of nominal strength according to the number of GFRP layers. For the size effect analysis of RC beams strengthened with FRP, additional parameters regarding the test data and numerical work are given in Table 1.

Size Effect Analysis

In the size effect analysis, the shear span (a) is chosen as the characteristic length of the FRP-reinforced beams. The main failure modes should not change with geometrically scaling according to the main principles of the size effect equation used in Eq. (5). Different failure modes require some modifications in the size effect law which is not considered here. Debonding cracking mainly occurs along the FRP length. The widths of the FRP plates in the tests, which are chosen to conduct the numerical work, are the same with the beam width b_w. The width of the FRP plates may be smaller than the beamwidth, which leads to less flexural rigidity than the case of full width. As the bending of structures in this study can be accepted as an in-plane loading case, narrower FRP width would not change the bending mechanism. Eq. (6) gives the strength definition for this type of failure. The geometric scaling of the FRP-strengthened RC beam requires proportional scaling of both the RC beam and the FRP reinforcement. The effects of the boundary layers are minimized by using a two-dimensional (2D), rather than three-dimensional (3D), scaling of the structures. Thus, the beam dimensions should be scaled while keeping the width, b_w, and the reinforcement ratio constant.

The predictions for larger sizes and a different number of FRP layers, based on calibrations by three different data sets, are shown in Fig. 6. The size effect specimens are simulated using the FE crack-band microplane model M7, for 2D geometrical scaling, up to four different sizes. All the layer numbers refer to the smallest specimen, and the number of the layers (or layer thickness) scales in proportion to specimen size. The values of σ_{N0} and D_0 are found through nonlinear regression. The given relative strength values are normalized by zero layer strength, σ_0. The cross marks refer to M7 predictions and the circle points to the test data. The dashed horizontal line refers to the strength of the control specimen (0 layers).

Fig. 6(a) presents the results of the size effect analysis for the first data set. Bažant's type 2 (Bažant 1984) size effect law matches the data for every delamination type and every number of layers.

Table 1. Parameters of the experimental data and numerical study used in size effect analysis

Test	1st data set	2nd data set	3rd data set	4th data set
Source	Maalej and Bian (2001)	Raoof and Bournas (2017)	Chiew et al. (2007)	Maalej and Leong (2005)
Test	4PB[a]	4PB	4PB	4PB
Figure(s)	Figs. 3 and 6(a)	Figs. 4 and 6(b)	Figs. 5 and 6(c)	Fig. 6(d)
Size range (tested)	D	D	D	$D/2D/3.2D$
Size range (FEA)[b]	$D/2D/4D/8D$	$D/2D/4D/8D$	$D/2D/4D/8D$	$D/2D/3.2D$
$h \times b_w$ [mm][c]	150×115	203×102	350×200	146×115[d]
ρ_s [%], d [mm]	1.36, 125	0.56, 176	0.63, 317	1.71, 120
a [mm] (a/d)	500 (4.0)	580 (3.3)	800 (2.52)	500 (4.17)
FRP type	CFRP[e]	CFRP	GFRP[f]	CFRP
Number of FRP layers	0/1/2/3/4	0/1/3[g]	0/1/2/3	0/1/2
t_f^h [mm] (for 1L)	0.111	0.095	1.7	0.165
E_f [GPa]	230	219	27	235
M7 parameters*	85×10^{-6}/85.0/30/65	75×10^{-6}/75.0/30/50	55×10^{-6}/55.0/31/55	64×10^{-6}/66.0/31/60
h_c^i (FE size) [mm]	20	27	25	12.5

[a]Four-point bending.
[b]Additional sizes are the predictions based on the calibration of the data sets.
[c]Here $h \times b_w$ are the cross-sectional dimensions and refer to total height and width of the concrete section.
[d]Corresponds to the smallest size, D.
[e]Carbon FRP.
[f]Glass FRP.
[g]Selected test data for small size.
[h]Thickness of size D.
[i]The smallest dimension of one finite element.

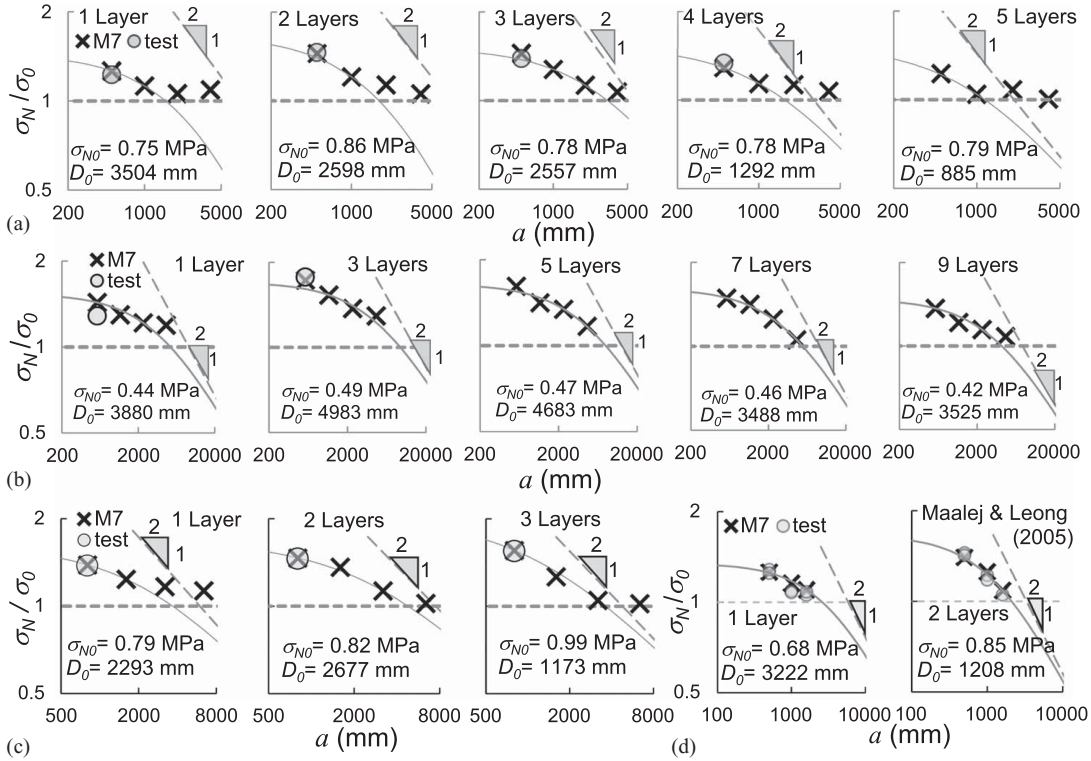

Fig. 6. Relative strength versus characteristic size plots of computed (cross) and test (circle) data on the double-log scale based on the calibration of (a) the first data set (Maalej and Bian 2001); (b) the second data set (Raoof and Bournas 2017); (c) the third data set (Chiew et al. 2007); and (d) simulation of the size effect tests by Maalej and Leong (2005) ($\sigma_0 = 0.51$ MPa). Corresponding SEL fits for various t_f values are shown as solid curves (note that the layer number, or t_f, shown on the curves correspond to the smallest specimens in each set which also scales with the beam size).

The ordinates, $\log\sigma_N/\sigma_{N0}$, represent the ratio of the nominal strength to that of a beam with no FRP. In other words, the size effect occurs only for the additional beam strength due to FRP reinforcement. As expected, the deviation from the SEL curve increases as the nominal strength of the beam approaches the horizontal dashed line $\sigma_N/\sigma_{N0} = 1$, indicating the strength of the beam with no FRP reinforcement.

The failure mode may switch to the failure mode of the control specimen or a different mode of delamination as the size increases. This depends on which part of the FRP reinforcement gets

debonded. For instance, for the IC debonding failure mode, the crack usually propagates from the middle to the FRP layer end. Therefore, some parts of the FRP reinforcement could still be active in the midspan region. This uncracked part of the beam contributes to the moment capacity of the base structure. Thus, the deviations from the SEL curve may start above the horizontal line as is usually seen in the case of one layer of FRP reinforcements. However, the nominal strength cannot go below the zero layer limit, because the governing failure mode of the control specimens is the yielding of steel followed by the crushing of concrete, in which the size effect is absent (or small, if the concrete is crushing, which should, of course, be precluded in design).

Figs. 6(b and c) show broader size predictions using the calibration of M7 based on the second and third data sets. The results of the size effect simulations are similar. In addition, the experimental verification of the size effect in this failure type was conducted in Maalej and Leong (2005). In this study, beams of three different sizes, with the size ratios of $D : 2D : 3.2D$, were analyzed with 3D scaling. The M7 simulations fit the test data adequately, as seen in Fig. 6(d).

All the predictions and tests document a significant size effect, which cannot be neglected in design.

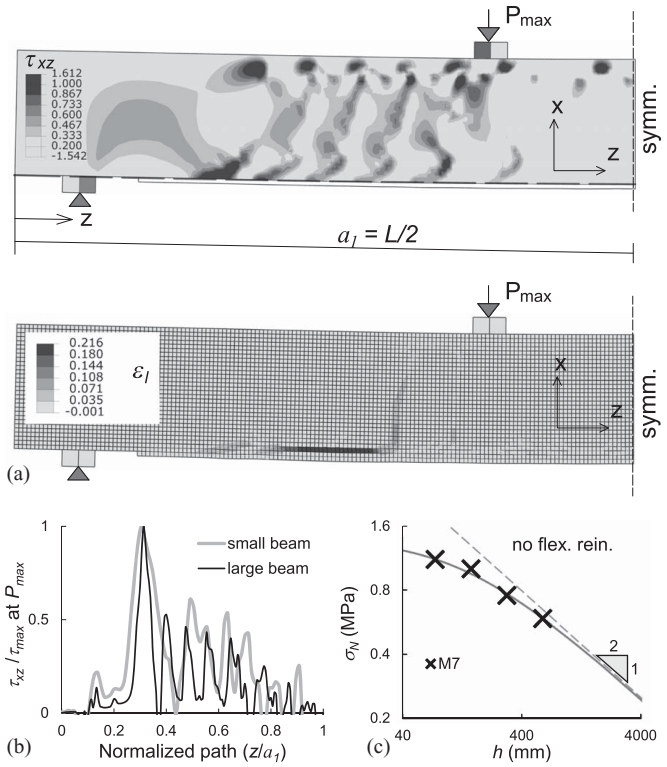

Fig. 7. (a) Numerical results demonstrate the shear stress contours and FE mesh with cracking pattern; (b) the variations of shear stress along the FRP–concrete interface for both large and small beams; and (c) size effect behavior for four different sizes of FRP-strengthened beams without steel reinforcement.

Discussion

The steel reinforcement obstructs the simplicity of the size effect curve, owing to a change of the failure mode for larger FRP strengthened beams. The simple curve of the SEL can be obtained by removing from the beams the flexural steel reinforcement (Fig. 7). Figs. 7(a and b) show the shear stress distribution along the length of concrete–FRP interface, for both small (size D) and large (size $2D$) beams, at the maximum load, P_{max}.

The failure mechanism is not the same as it is for the SST specimens in Fig. 2. As the beam bends, tensile stresses in the cross-section below the neutral axis increase. As the tensile strength of concrete is relatively low, the flexural cracks propagate towards the neutral axis, whose location moves as the cross-sectional stresses change. The shear forces in these cracked sections transfer into the FRP–concrete interface, creating a sharp shear stress concentration. Further bending of the beam creates new cracks and sharp shear stress concentrations next to each other, with slightly inclined orientations due to shear cracking effects, as shown in Figs. 7(a and b). The failure occurs when several adjacent segments (or toothlike segments of the concrete cover) coalesce to form a debonding zone with an abrupt load drop. The number of coalescing segments depends on the balance between the strain energy released and the energy dissipated by fracture. Therefore, large beams with thin FRP reinforcement may fail even by the debonding of one segment. That is the source of the early deviation from the SEL in one layer of the FRP-strengthened specimens (Fig. 6).

On the other hand, the highest energy release can be achieved in small beams with fewer numbers of layers. However, these types of interface debonding usually do not occur exactly at the FRP–concrete interface because the FRP stiffness provides high confinement on the neighboring concrete layer. Therefore, the elements above the interface layer, which have weaker confinement, can initiate the delamination fracture by leaving concrete debris on the FRP inner surface.

The texture of the toothlike segments in the concrete cover does not change with size. The failure mode and location of the cracking initiation are the same for geometrically scaled structures, as shown in Fig. 7(c). The stress states at the homologous points are similar for large and small beams, and the SEL fits the data without any horizontal limit. Therefore, the FPZ can be regarded as constant

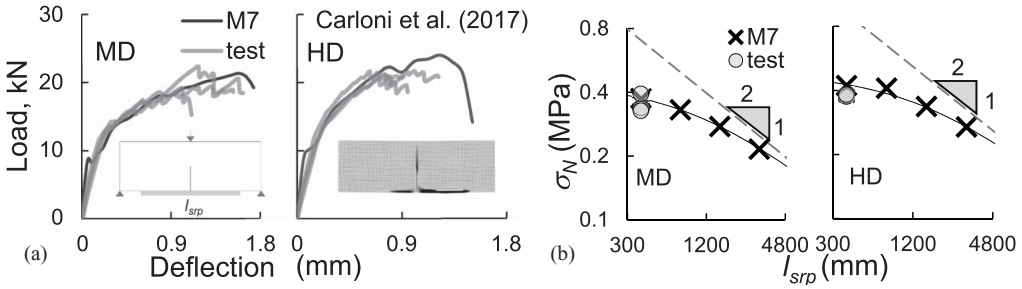

Fig. 8. (a) The calibration of M7 using the three point bending test of strengthened notched beams in Carloni et al. (2017); and (b) prediction for larger sizes and the size effect trend of concrete prisms reinforced with SRP plates on the tension face.

for geometrically scaled beams. What matters is the relative stiffness value or the ratio of the stiffness of the unreinforced and FRP-strengthened cases, ξ in Eq. (7), which does not change with 2D or 3D scaling. These facts make the failure mechanisms of FRP-strengthened beams different from the SST specimens.

Another validation of the uniform trend of size effect without steel reinforcement is provided by Fig. 8, showing the test data of Carloni et al. (2017). The concrete prisms of dimensions $150 \times 150 \times 600\,\text{mm}^3$ and with a half-depth notch are subjected to three-point bending. The specimens are strengthened with steel fiber-reinforced polymer (SRP) composites on their tension face. Two different SRP plates are used in these tests. MD in Fig. 8 refers to the medium density of steel strips whereas HD refers to high density, which corresponds to two different equivalent thicknesses of the bonded plates. The calibration of M7 is based on the load versus midspan deflection behavior of the tests for both MD and HD specimens, as shown in Fig. 8(a). The prediction for larger sizes is shown in Fig. 8(b). Similar to the results displayed in Fig. 7(c), the numerical results exhibit a clear size effect trend.

Conclusions

The results of this study, which deals with an important problem of the size effect on externally bonded FRP systems for strengthening concrete structures, are shown to be applicable to both the FRP sheets (cured in situ) and the laminates (pre-cured pultruded systems) used to strengthen beams or slabs in flexure. For the shear strengthening of RC beams or slabs, the size effect factor for beam shear, recently introduced into ACI-318 design code, must also be applied.

Although the restraint of FRP by the bonded concrete prevents cracking just next to the bonded FRP surface, cracking generally develops deeper in the concrete substrate than the bond surface.

Geometrically scaled FRP-strengthened RC beams exhibit a significant energetic size effect. However, the size effect applies only to the additional beam strength owing to the FRP reinforcement. Deviations from the energetic SEL occur for large sizes for which the nominal strength of the beam approaches the nominal strength owing to the flexural steel reinforcement alone. This is the strength of the case of no FRP strengthening.

The differences among the delamination failure modes can be attributed to the ratio, ξ, of the bending stiffnesses of steel and FRP reinforcement. Increasing the thickness of FRP sheets makes ξ larger and shifts the fracture initiation towards the FRP end. The competition between the failure modes of delamination is determined by the relative importance of tensile and shear stresses for the fracture initiation.

Placing the end (or cutoff point) of the FRP sheet inside the shear span of the FRP-reinforced beam changes the failure mode for higher FRP thicknesses to the cover delamination. The stress concentration at the cutoff point causes ripping off the concrete at the cutoff point, which triggers delamination failure and lowers the beam strength values. FRP sheet designs extending slightly beyond the point of delamination could help to avoid this type of failure.

Eq. (5) can be used to define the strength of the debonding failures of the FRP–concrete interface. The size effect factor in this equation is denoted as λ_s. The shear span, a, should be used in λ_s as the characteristic structure size. For smaller sizes, the beam strength is, in Eq. (6), defined as a function of the concrete compressive strength f_c, and the ratio, ξ, of the bending stiffnesses of the FRP sheet and the steel reinforcements.

The effective length concept for the SST specimens cannot be applied directly to the RC beam problems. The failure and energy release mechanism of a bending specimen is different than it is in direct shear failures. Moreover, the geometrical scaling of an FRP-reinforced member under flexure does not change the FPZ in debonding failures, whereas in SST, the FPZ changes depending on the axial stiffness of FRP (or another elastic material). The FPZ of debonding cracks in the RC beam is much longer than the FPZ in SST. More importantly, the initial flexural and shear-flexural cracks in the shear zone create in the concrete cover small toothlike segments, and these segments further prevent the shear zone length from reaching the full effective length.

Data Availability Statement

- Some or all data, models, or code generated or used during the study are available in a repository online in accordance with funder data retention policies (http://www.civil.northwestern.edu/people/bazant/s).

Acknowledgments

The first author thanks ITU BAP for supporting the Project No. 40860 and The Scientific and Technological Research Council of Turkey for financially supporting the first 12 months of his post-doctoral appointment at Northwestern University. Partial funding under NSF Grant No. CMMI-2029641 to Northwestern University is gratefully acknowledged.

References

ACI (American Concrete Institute). 2017. *Guide for the design and construction of externally bonded FRP systems for strengthening concrete structures*. Rep. No. 440.2R-17. West Lafayette, IN: ACI.

Arduini, M., and A. Nanni. 1997. "Behavior of precracked RC beams strengthened with carbon FRP sheets." *J. Compos. Constr.* 1 (2): 63–70.

Attari, N., S. Amziane, and M. Chemrouk. 2012. "Flexural strengthening of concrete beams using CFRP, GFRP and hybrid FRP sheets." *Constr. Build. Mater.* 37: 746–757.

Bažant, Z. P. 1984. "Size effect in blunt fracture: Concrete, rock, metal." *J. Eng. Mech.* 110 (4): 518–535.

Bažant, Z. P. 2002. *Scaling of structural strength*. London: Hermes Penton Science.

Bažant, Z. P., and B. H. Oh. 1983. "Crack band theory for fracture of concrete." *Matér. Constr.* 16 (3): 155–177.

Bažant, Z. P., and J. Ožbolt. 1990. "Nonlocal microplane model for fracture, damage, and size effect in structures." *J. Eng. Mech.* 116 (11): 2485–2505.

Bažant, Z. P., and J. Planas. 1998. *Fracture and size effect in concrete and other quasibrittle materials*. Boca Raton, FL: CRC Press.

Brena, S. F., R. M. Bramblett, S. L. Wood, and M. E. Kreger. 2003. "Increasing flexural capacity of reinforced concrete beams using carbon fiber-reinforced polymer composites." *Struct. J.* 100 (1): 36–46.

Caner, F. C., and Z. P. Bažant. 2013a. "Microplane model m7 for plain concrete. I: Formulation." *J. Eng. Mech.* 139 (12): 1714–1723.

Caner, F. C., and Z. P. Bažant. 2013b. "Microplane model m7 for plain concrete. II: Calibration and verification." *J. Eng. Mech.* 139 (12): 1724–1735.

Carloni, C., M. Santandrea, and I. A. O. Imohamed. 2017. "Determination of the interfacial properties of SRP strips bonded to concrete and comparison between single-lap and notched beam tests." *Eng. Fract. Mech.* 186: 80–104.

Carrara, P., D. Ferretti, F. Freddi, and G. Rosati. 2011. "Shear tests of carbon fiber plates bonded to concrete with control of snap-back." *Eng. Fract. Mech.* 78 (15): 2663–2678.

Chen, J. F., and J. G. Teng. 2001. "Anchorage strength models for FRP and steel plates bonded to concrete." *J. Struct. Eng.* 127 (7): 784–791.

Chiew, S.-P., Q. Sun, and Y. Yu. 2007. "Flexural strength of RC beams with GFRP laminates." *J. Compos. Constr.* 11 (5): 497–506.
Dönmez, A., and Z. P. Bažant. 2017. "Size effect on punching strength of reinforced concrete slabs with and without shear reinforcement." *ACI Struct. J.* 114 (4): 875–886.
Dönmez, A., and Z. P. Bažant. 2019. "Critique of critical shear crack theory for FIB model code articles on shear strength and size effect of reinforced concrete beams." *Struct. Concr.* 20 (4): 1451–1463.
Maalej, M., and Y. Bian. 2001. "Interfacial shear stress concentration in FRP-strengthened beams." *Compos. Struct.* 54 (4): 417–426.
Maalej, M., and K. S. Leong. 2005. "Effect of beam size and FRP thickness on interfacial shear stress concentration and failure mode of FRP-strengthened beams." *Compos. Sci. Technol.* 65 (7–8): 1148–1158.
Raoof, S. M., and D. A. Bournas. 2017. "TRM versus FRP in flexural strengthening of RC beams: Behaviour at high temperatures." *Constr. Build. Mater.* 154: 424–437.
Rasoolinejad, M., and Z. P. Bažant. 2019. "Size effect of squat shear walls extrapolated by microplane model M7." *ACI Struct. J.* 116 (3): 75–84.
Saadatmanesh, H., and M. R. Ehsani. 1991. "RC beams strengthened with GFRP plates. I: Experimental study." *J. Struct. Eng.* 117 (11): 3417–3433.
Teng, J. G., S. T. Smith, J. Yao, and J. F. Chen. 2003. "Intermediate crack-induced debonding in RC beams and slabs." *Constr. Build. Mater.* 17 (6–7): 447–462.